LA-UR-21-28802

Accepted Manuscript

Understanding effects of chemical complexity on helium bubble formation in Ni-based concentrated solid solution alloys based on elemental segregation measurements

Wang,Xing
Jin, Ke
Wong, Chun-Yin
Bei, Hongbin
Wang, Yongqiang
Ziatdinov, Maxim
Weber, William J.
Zhang, Yanwen
Poplawsky, Jonathan
More, Karren L.

Provided by the author(s) and the Los Alamos National Laboratory (2022-07-05).

To be published in: Journal of Nuclear Materials

DOI to publisher's version: 10.1016/j.jnucmat.2022.153902

Permalink to record:

http://permalink.lanl.gov/object/view?what=info:lanl-repo/lareport/LA-UR-21-28802







Los Alamos National Laboratory, an affirmative action/equal opportunity employer, is operated by Triad National Security, LLC for the National Nuclear Security Administration of U.S. Department of Energy under contract 89233218CNA000001. By approving this article, the publisher recognizes that the U.S. Government retains nonexclusive, royalty-free license to publish or reproduce the published form of this contribution, or to allow others to do so, for U.S. Government purposes. Los Alamos National Laboratory requests that the publisher identify this article as work performed under the auspices of the U.S. Department of Energy. Los Alamos National Laboratory strongly supports academic freedom and a researcher's right to publish; as an institution, however, the Laboratory does not endorse the viewpoint of a publication or guarantee its technical correctness.

Understanding effects of chemical complexity on helium bubble formation in Ni-based concentrated solid solution alloys based on elemental segregation measurements

Xing Wang, Ke Jin, Chun-Yin Wong, Di Chen, Hongbin Bei, Yongqiang Wang, Maxim Ziatdinov, William J. Weber, Yanwen Zhang, Jonathan Poplawsky, Karren L. More

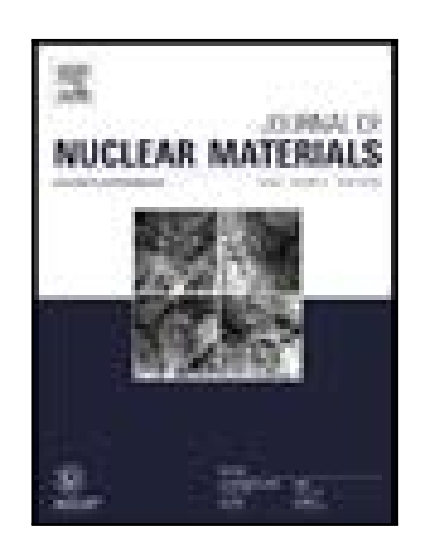
PII: \$0022-3115(22)00388-9

DOI: https://doi.org/10.1016/j.jnucmat.2022.153902

Reference: NUMA 153902

To appear in: Journal of Nuclear Materials

Received date: 5 April 2022 Revised date: 30 June 2022 Accepted date: 1 July 2022



Please cite this article as: Xing Wang, Ke Jin, Chun-Yin Wong, Di Chen, Hongbin Bei, Yongqiang Wang, Maxim Ziatdinov, William J. Weber, Yanwen Zhang, Jonathan Poplawsky, Karren L. More, Understanding effects of chemical complexity on helium bubble formation in Ni-based concentrated solid solution alloys based on elemental segregation measurements, *Journal of Nuclear Materials* (2022), doi: https://doi.org/10.1016/j.jnucmat.2022.153902

This is a PDF file of an article that has undergone enhancements after acceptance, such as the addition of a cover page and metadata, and formatting for readability, but it is not yet the definitive version of record. This version will undergo additional copyediting, typesetting and review before it is published in its final form, but we are providing this version to give early visibility of the article. Please note that, during the production process, errors may be discovered which could affect the content, and all legal disclaimers that apply to the journal pertain.

© 2022 Published by Elsevier B.V.

Understanding effects of chemical complexity on helium bubble formation in Ni-based concentrated solid solution alloys based on elemental segregation measurements

Xing Wang,^{1,2}* Ke Jin,³ Chun-Yin Wong,⁴ Di Chen,^{5,6} Hongbin Bei,³ Yongqiang Wang,⁵ Maxim Ziatdinov,^{4,7} William J. Weber,^{8,3} Yanwen Zhang,^{3,8} Jonathan Poplawsky,¹ and Karren L. More¹*

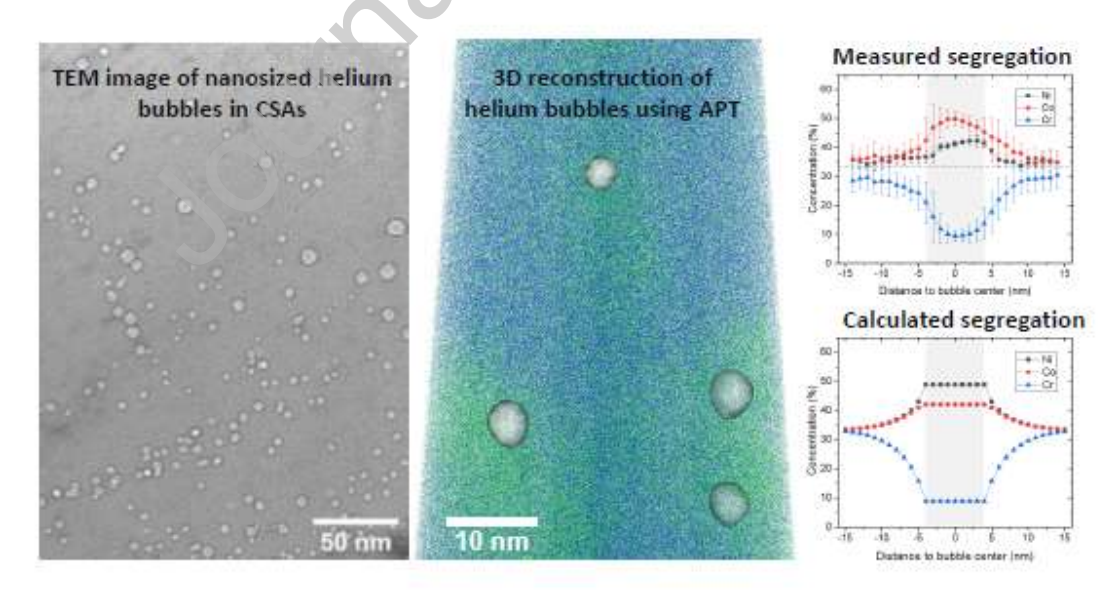
- 1. Center for Nanophase Materials Sciences, Oak Ridge National Laboratory, Oak Ridge, TN, USA
- 2. Department of Nuclear Engineering, Pennsylvania State University, University Park, PA, USA
- 3. Materials Science and Technology Division, Oak Ridge National Laboratory, Oak Ridge, TN, USA
- 4. The Bredesen Center, University of Tennessee Knoxville, Knoxville, TN, USA
- 5. Materials Science and Technology Division, Los Alamos National Laboratory, Los Alamos, NM. USA
- 6. Department of Physics & Texas Center for Superconductivity, University of Houston, Houston, TX, 77204, USA
- 7. Computing and Computational Sciences Directorate, Oak Ridge National Laboratory, Oak Ridge, TN, USA
- 8. Department of Materials Science and Engineering, University of Tennessee Knoxville, Knoxville, TN, USA
- * Corresponding authors

Contact information of the corresponding author Xing Wang

Email: <u>xvw5285@psu.edu</u> Phone: +1 (814) 863-0413

Address: 223 Hallowell Building, University Park, PA, USA 16802

Graphical abstract



Abstract

Helium bubble formation and swelling were systematically studied in Ni-based concentrated solid solution alloys containing different numbers and types of elements. Our microscopy analysis showed that although increasing the alloy chemical complexity helps suppress bubble formation in general, there is no monotonic relationship between the bubble growth rate and the number of alloying elements. Certain elements (e.g., Fe and Pd) are more effective in suppressing bubble growth than others (e.g., Cr and Mn). Atom probe tomography was applied to accurately measure elemental segregation around bubbles, revealing unique effects of certain alloying elements on vacancy migration towards bubbles. More specifically, the high vacancy mobility via Cr sites leads to a large vacancy flux and an increased bubble size, while the high degree of atomic size mismatch introduced by Pd helps deflect vacancy flow away from bubbles and decrease the amount of swelling. The effects identified in this study provide new strategies to design concentrated solid solutions with superior resistance to swelling.

Keywords

Irradiation effect; Segregation; High entropy alloys; Atom probe tomography (APT)

1. Introduction

Designing materials with superior resistance to radiation damage has been a long-standing goal for the nuclear materials community. In the past two decades, researchers have shown that exploiting the structural complexity of materials is a promising approach to reach this goal. By introducing structural heterogeneities, such as phase boundaries and precipitate interfaces that serve as defect sinks in the materials, radiation-tolerant nanolayered composites and oxide dispersion-strengthened steels have been developed [1,2]. Recently, another promising approach has emerged that aims at optimizing the chemical complexity of materials. An example are concentrated solid solution alloys (CSAs) [3–6], which are formed by mixing multiple elements in equal or nearly equal concentrations. CSAs are also referred to as high entropy alloys (HEAs) if five or more elements are mixed or as medium entropy alloys (MEAs) with three or four elements. In CSAs, different elements are randomly accommodated in a simple crystal structure, such as face-centered cubic (fcc), creating a unique distortion for each lattice site and a chemically complicated environment around each atom [5,6]. Studies have shown that chemical complexity can be used to effectively tune the defect energy landscape, promote defect recombination, and

improve the radiation resistance of materials [7,8]. A more chemically complicated alloy means there are more possible arrangements of atoms in the alloy with larger variations in local electronic and atomic structures. The chemical complexity of CSAs is primarily controlled by the number, type, and concentration of elements in the alloy [5,6,9], and often increases as the number of alloying elements increases and as the alloy composition approaches equi-atomic, but this may not always be the case [10].

The formation of helium (He) bubbles is a major threat to the integrity of materials under irradiation. Neutron bombardment of solids produces point defects by collision cascades and generates He atoms by nuclear transmutation reactions. Because of the extremely low solubility in most solids, He atoms quickly cluster with vacancies to form He-stabilized voids or pressurized bubbles, both of which degrade materials' mechanical and thermal properties [11]. Void or bubble formation and the ensuing swelling are often used as standards to compare the radiation tolerance of different materials. A few studies have discovered that increasing the alloy chemical complexity can effectively suppress bubble formation and swelling. Two research teams independently confirmed that the average bubble size in FeCoNiCr was smaller than that in pure Ni subjected to the same irradiation condition [12,13]. In $Ni_{(I-x)}Fe_x$ alloys, the bubble growth rate decreased as the Fe concentration x increased from 0 at. % to 50 at. % [14], which is consistent with recent modeling studies that showed increasing the Fe concentrations up to 70 at. % led to higher chemical complexity in $Ni_{(I-x)}Fe_x$ alloys [10]. However, there is not always a monotonic trend between the number of elements in the alloys and their resistance to swelling. Jin et al. found that the void swelling was less than 0.20 % in NiCoFe but was about 0.33 % in NiCoFeCr [15]. A comparison between He bubbles in a series of $Ni_{0.8}X_{0.2}$ alloys, where X can be Co, Fe, Cr, Pd or Mn, showed that the bubble size was smallest in Ni_{0.8}Mn_{0.2}, suggesting that certain alloying elements may play

a more dominant role in suppressing bubble growth [16]. To design CSAs with superior radiation resistance, it is necessary to fully understand how the local electronic and atomic structures of CSAs are modified by the alloying elements as well as the mechanisms by which chemical complexity suppresses bubble formation.

In this work, we studied bubble formation in two quinary HEAs, NiCoFeCrMn and NiCoFeCrPd, two ternary MEAs, NiCoFe and NiCoCr, as well as the binary NiFe and pure Ni irradiated under the same condition. Since all the alloys are equi-atomic, the concentration subscriptions are omitted. For simplicity, NiCoFeCrMn is referred to as Mn-HEA and NiCoFeCrPd is referred to as Pd-HEA hereafter. The direct comparisons between multiple CSAs enabled us to elucidate the effects of both the number and type of alloying elements on the bubble formation process. A major driving force for bubble growth is vacancy flux towards bubble surfaces. Since vacancies usually prefer to diffuse via certain alloying elements, the vacancy flux is often non-stoichiometric, leading to either enrichment or depletion of specific elements around bubbles [17-19]. Therefore, analyzing elemental segregation is helpful for revealing key defect kinetics during bubble growth. With recent progresses in atom probe tomography (APT), we were able to characterize elemental segregation around bubbles in HEAs and MEAs with high accuracy [20]. Using ab initio informed-rate theory calculations, some trends of elemental segregation observed experimentally were reproduced and the different roles of alloying elements during bubble growth were identified. Based on the analyses, we explained why He bubble formation was more effectively suppressed in certain CSAs and provided new insights for designing CSAs with improved resistance to swelling.

2. Experimental Methods

2.1. Bulk sample fabrication and irradiation

All the alloys in this study were synthesized by arc melting and drop casting using elemental metals with >99.9% purity. Single-crystal rods of Ni and alloys (except two HEAs) were grown using a floating-zone directional solidification method [21]. The two HEAs were prepared using the same method but are single-phase polycrystals with an average grain size larger than 4 µm. Laue X-ray backscatter diffraction was used to confirm the alloys were single-phase fcc solid solution with good single-crystal quality [9]. To generate He bubbles, bulk specimens were irradiated by 200 keV He⁺ ions from a 200 kV Danfysik Research Ion Implanter at the Ion Beam Materials Laboratory in Los Alamos National Laboratory. The He beam flux was about 2×10¹³ ions/(cm²·s) and the total fluence was 5×10¹⁶ ions/cm². During irradiation, the specimen temperature was maintained at 500 °C and monitored using thermocouples. 500 °C was chosen here because it is close to the swelling peak temperature shown in ion-irradiated Ni with dose rates from 8×10⁵ dpa/s to 1.6×10⁻³ dpa/s [22]. As shown in Section 3.1, the dose rate in our experiment was 3.2×10⁻⁴ dpa/s, so we expected obvious cavity formation that would facilitate the post-irradiation examination. The specimens were heated to the desired temperature at a rate of 0.33°C/s before irradiation and were naturally cooled down to room temperature after the irradiation.

2.2. Transmission electron microscopy characterization of bubbles

Transmission electron microscopy (TEM) was used to image He bubbles and dislocations in the irradiated specimens. To conduct TEM analysis, thin lamellas (~ 120 nm thick) were prepared by the standard focused-ion beam (FIB) lift-out procedure using an FEI Nova 200 dual-beam FIB. It is known that FIB thinning causes artificial damages on lamella surfaces that may interfere with TEM analyses of radiation-induced defects [23]. Therefore, flash-electropolishing was performed right after the FIB thinning to remove about 20 nm on both sides of the lamella [24]. TEM analysis was conducted using a 300 kV FEI Titan S instrument. He bubbles were characterized using the

through-focus technique based on Fresnel contrast mechanism. Specifically, bubbles appeared as bright spots in under-focused condition and as dark spots in the over-focused condition. Dislocations were characterized using two-beam imaging conditions in bright field (BF) TEM images.

To obtain reliable statistics regarding bubble sizes and densities, a convolutional neural network model was developed to automatically measure bubbles in the TEM images, enabling us to analyze a large number of bubbles and minimize human bias. This model is based on the U-Net structure for microscopy image segmentation [25]. A brief introduction to this model is provided in Supplementary Note 1. To calculate the volume swelling introduced by bubble formation, the thickness of each lamella was measured using electron energy loss spectroscopy (EELS) spectrum imaging performed in the same Titan microscope but operated in the scanning transmission electron microscopy (STEM) mode. The uncertainty of calculated swelling mostly comes from the uncertainty of the sample thicknesses (~ ±10 %) measured using the EELS method [26].

2.3. APT measurement of elemental segregation

Elemental segregations near bubbles were characterized using APT. Although STEM-based analytical methods, including EELS and energy dispersive X-ray spectroscopy (EDS) are powerful tools for measuring local composition, these methods suffer from an intrinsic limitation for nanosized structures embedded in the specimen, e.g., bubbles. Since the electron beam must pass through the specimen during EELS or EDS analysis, the measured composition is actually the average value along the entire beam path (i.e., specimen thickness). Depending on the bubble size and the specimen thickness, the averaging effect can introduce large errors in the measurement, preventing quantitative comparisons of elemental segregations around bubbles between different specimens. An illustration of this averaging effect is provided in Supplementary Note 2. Compared

to EELS or EDS, APT quantifies the local compositions in 3D with a much higher chemical sensitivity (~ 10 parts per million) [27]. During the APT experiment, high-voltage pulses and/or laser pulses are constantly applied to a needle-shaped specimen and individual atoms are ionized and extracted from the specimen surface one-by-one, i.e., field evaporation. The ionized atoms are captured by a position-sensitive detector. The 3D coordinates of each atom are reconstructed based on its impact position on the detector and the order of evaporation, while the ion identity (i.e., its mass-to-charge ratio) is determined based on its time of flight. In this way, APT provides much more accurate measurements of elemental segregations near nanosized bubbles than STEM-based EELS or EDS without the averaging effects [20]. Fig. 1 shows an example of an APT reconstruction of a NiFe specimen containing He bubbles. Bubble locations can be identified by local atomic density variations in the APT reconstruction [20]. For alloys in this study, bubbles exhibit as high-density regions, which are marked by white iso-density surfaces in Fig.1. Once the bubble locations are identified, we can define either a cylindrical region-of-interest (ROI) passing through the bubble to extract a 1D concentration profile, or a thin slab-shaped ROI around the bubble to obtain the 2D elemental distribution map (Fig.1b). All the cylindrical ROIs in this study were set to parallel to the z-axis to eliminate the potential influence of ROI orientation on the measured concentration profiles. A CAMECA LEAP 4000X HR system was used here for APT data acquisition. The APT field evaporation was conducted in laser mode with a specimen temperature of 45 K, a pulse repetition rate of 200 kHz, a detection rate of 0.004 atoms per pulse, and 70 pJ laser energy. For each alloy, two APT specimens were analyzed. More than five million atoms were collected, and multiple bubbles were identified in each specimen. The obtained APT data was analyzed using IVAS 3.8.3 software.

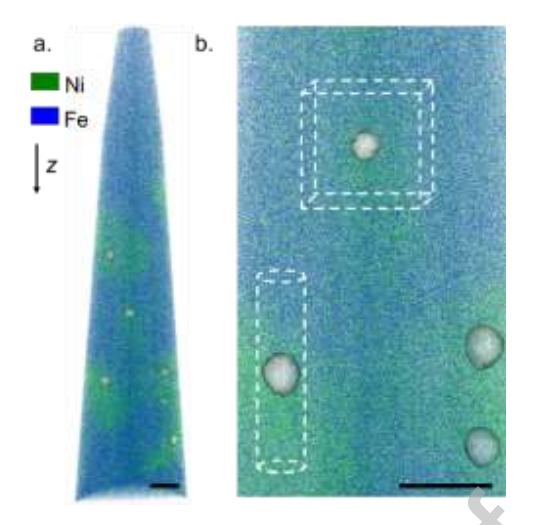


Figure 1. Measuring elemental segregation near bubbles using APT. (a) APT reconstruction showing bubbles identified by white iso-density surfaces. (b) ROIs passing through bubbles for calculating 1D concentration profiles and 2D concentration maps around bubbles. Scale bars in both images are 10 nm.

3. Results and Discussions

3.1. Comparison of bubble growth in CSAs and Ni

The distribution of implanted He and the radiation damage profile were calculated using the Stopping and Range of Ions in Matter (SRIM) package (2013 version) [28]. The calculated results are summarized in Supplementary Note 3 with details of the calculation. As shown by the SRIM results, the profiles of radiation damage and He distribution are quite similar as the atom densities of studied CSAs and Ni are very close. The He concentration peak is located around 400 nm – 620 nm below the sample surface with a He concentration >1.0 at.%. TEM analysis found that such a high He concentration led to very dense and small bubbles concentrating at the peak, making it challenging to quantitatively compare bubble density and size at this location between different CSAs. TEM images showing the bubbles at the peak are provided in Supplementary Note 4. Therefore, we focused on the region 50 nm – 350 nm below the sample surface in this study, where the implanted He concentration is lower (0.03 at. % - 0.50 at. %) and the damage profile is

relatively flat with the average dose of 0.8 dpa and dose rate of 3.2×10⁻⁴ dpa/s. Obvious differences in bubble sizes between different alloys were observed in this region.

Fig. 2 compares the size of He bubbles in six studied materials between 50 nm and 350 nm below the sample surface. All the BF-TEM images are at the same magnification and were acquired at similar under-focus conditions (defocus=0.2-0.5µm). It is clear that bubbles in different alloys exhibit different characteristics. For example, large bubbles are easily observed in Ni and NiCoCr but are barely found in NiCoFe or NiCoFeCrPd. Quantitative analysis was conducted based on statistics of more than 900 bubbles in each material. Histograms showing the bubble size distribution are presented in Fig. 3 and related statistical values are summarized in Table 1. Three trends are observed. First, the average bubble diameter (D_{bubble}) in Ni is larger than that of all the CSAs. According to Table 1, the ranking of average D_{bubble} in the six materials is Ni > NiCoCr > NiCoCrFeMn > NiFe > NiCoFe > NiCoCrFePd. Second, when looking at the histograms in Fig.3, we notice that in some CSAs such as NiFe and NiCoCr, there is a peak corresponding to small bubble diameter ($D_{bubble} = 3-4$ nm), but such a peak is not obvious in pure Ni, suggesting that the alloy chemical complexity slows down the rate of small bubbles growing into large ones. This trend is also observed in Table 1, which lists the fractions of small bubbles ($D_{bubble} < 4$ nm) and large bubbles ($D_{bubble} > 6$ nm) in all six materials. Compared to Ni, all the CSAs have a higher fraction of small bubbles and a lower fraction of large bubbles. Third, although chemical complexity suppresses bubble growth in general, there is no monotonic relationship between bubble size and the number of alloying elements. For example, the average D_{bubble} of NiFe is 4.5 nm, which is much smaller than that in NiCoCr with D_{bubble} =5.4 nm. Also, comparing two HEAs, despite having the same number of elements, bubbles in Pd-HEA are much smaller than Mn-HEA. Note that as shown in Fig. 2, more bubbles appear as faceted in NiCoCr and NiCoFe than the other

materials. According to the literature, a few factors, including the internal He pressure, the surface energies, as well as the anisotropic mechanical properties of the alloy, can affect the shape of bubbles [29,30]. Meanwhile, we should remind ourselves that the appearance of bubbles (i.e., spherical vs. faceted) in TEM images depends on the crystal orientation of the TEM sample [31,32]. Our previous work showed that the bubbles in NiFe were faceted when viewed along the <110> direction [33]. In addition, the faceting phenomenon has been observed in bubbles with a wide range of internal He pressure and bubble sizes in different alloys [29,31]. Therefore, for the following analyses in this work, we did not distinguish faceted and spherical bubbles. Future research is necessary to fully understand the bubble faceting in the Ni-based CSAs.

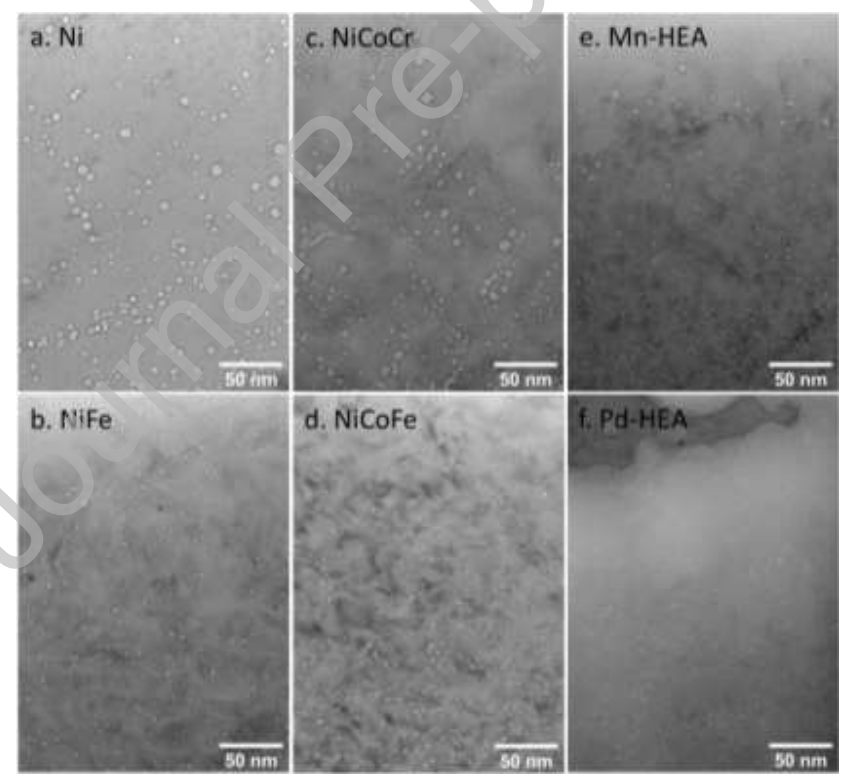


Figure 2. Under-focus BF-TEM images showing the bright Fresnel contrast from bubbles in Ni and five CSAs. For each image, the top edge of the image is about 50 nm below the irradiated sample surface and the bottom edge is about 350 nm below the surface.

We also quantified bubble-induced swelling in these materials. Here swelling is calculated by dividing the total bubble volume by the material volume shown in the TEM images. More details about the sample volume and thickness measurement are provided in Supplementary Note 5. The swelling of different alloys is summarized in Table 1. Larger average bubble diameters typically correlate with greater swelling. Therefore, although in general a higher alloy chemical complexity increases the alloy resistance to swelling, there is no monotonic relationship between swelling and number of alloying elements. The element type plays a more critical role in controlling bubble growth and swelling in CSAs. Specifically, a comparison between two MEAs (i.e., NiCoCr vs. NiCoFe) shows that alloying with Fe is more efficient than Cr in suppressing bubble growth and swelling. A similar comparison between two HEAs (i.e., NiCoCrFePd vs. NiCoCrFeMn) suggests that Pd is a better element than Mn to improve swelling resistance. These conclusions are further supported if we compare Mn-HEA to NiFe or NiCoFe. As Cr and Mn are added to the HEA, the swelling of this alloy becomes substantially larger. In the following two sections, we will focus on understanding the effect of different alloying elements on bubble growth process in CSAs.

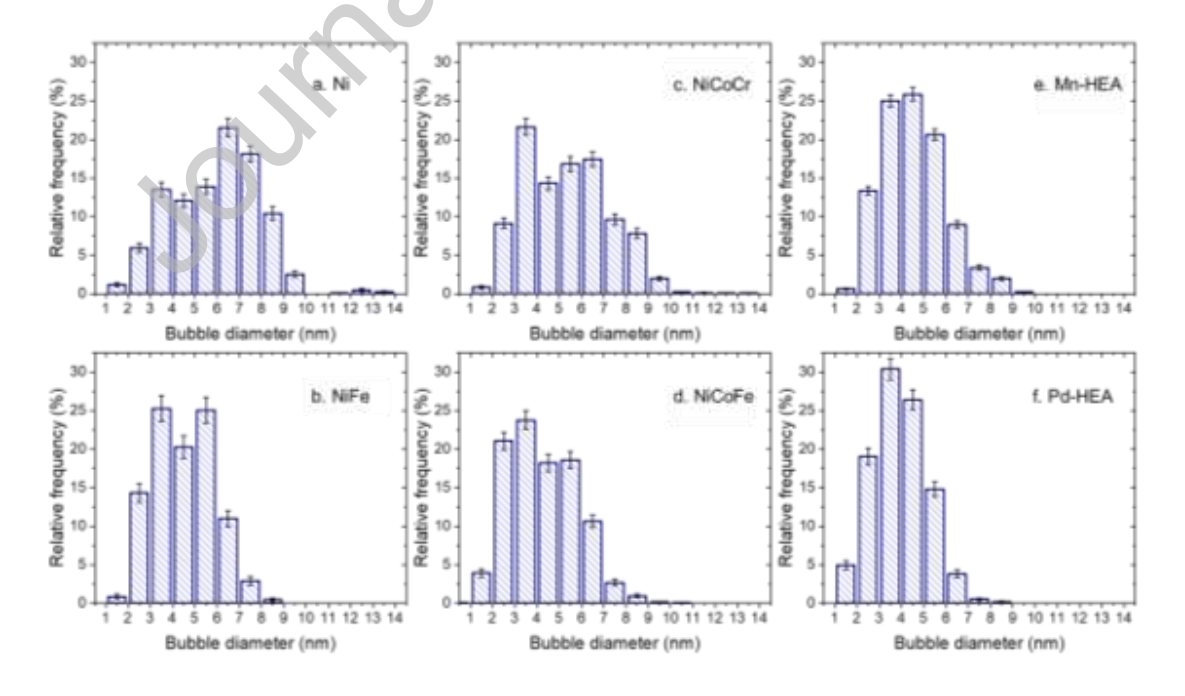


Figure 3. Comparison of bubble size distribution in Ni and five CSAs. Square root of bubble number count in each bin is taken as measurement uncertainty for calculating the error bar of relative frequency.

Table 1. Comparison of the average bubble diameters, swelling, fractions of small and large bubbles, bubble densities, and average dislocation loop sizes in Ni and CSAs

Materials	Ni	NiFe	NiCoCr	NiCoFe	Mn-HEA	Pd-HEA
Average bubble diameter (nm)	5.9	4.5	5.4	4.3	4.6	3.9
Swelling (%)	0.88 ± 0.09	0.39±0.04	0.81±0.08	0.30 ± 0.03	0.65±0.07	0.32±0.03
Fraction of small bubbles (%)	20.6±0.6	40.4±0.8	31.6±0.6	48.8±0.5	39.0±0.4	54.3±0.5
Fraction of large bubbles (%)	53.4±0.5	14.3±0.8	37.3±0.5	14.4±0.6	14.5±0.4	4.5±0.4
Total bubble density (nm ⁻³)	6.06×10 ⁻⁵	6.34×10 ⁻⁵	7.33×10-5	5.25×10 ⁻⁵	9.97×10 ⁻⁵	1.23×10 ⁻⁴
Ave. dislocation loop size (nm)	62±25	34±11	35±17	30±9	15±8	8±3

3.2. Chemical segregation near bubbles in MEAs

Bubbles grow by absorbing vacancies and He atoms from the alloy matrix. For alloys irradiated under the same condition, a higher vacancy diffusivity will lead to a larger incoming vacancy flux and a faster bubble growth rate. Vacancies migrate by switching positions with lattice atoms. If vacancies prefer a certain element for migrating, this element will become depleted around bubbles as the vacancy flux towards bubbles will transport the element away. The faster vacancies diffuse via this element, the larger the depletion of this element will be. Therefore, an accurate characterization of chemical segregation around bubbles can reveal the elemental effects on vacancy mobility and the kinetics of bubble growth.

Here, we compared the elemental segregations in two MEAs using APT analyses. As shown in Fig. 1, cylindrical ROIs ~5 nm in diameter passing through the iso-density surfaces were used to generate 1D composition profiles across the bubbles. To obtain a representative elemental

distribution, we selected five bubbles of similar sizes (diameter D_{bubble} =5-9 nm) in each MEA and calculated the average concentration profiles. To normalize the influence of different bubble sizes, we multiplied the x-axis of the concentration profiles by a factor of 8 nm/ D_{bubble} , resizing the profile as if it were from a bubble 8 nm in diameter. The averaged profiles in NiCoCr and NiCoFe are plotted in Fig.4a and 4b, respectively. It is worth noting that during field evaporation in APT experiments, atoms close to the bubble surface (within ~ 2 nm) experienced a strong ion trajectory aberration such that those atoms were falsely reconstructed into the bubble, which should be a cavity filled with only He atoms [20]. Because of this aberration, matrix elements were detected in the bubble region, i.e., -4 nm to 4 nm in Fig. 4. The concentration inside the bubble region can be interpreted as the average elemental concentrations of a 2 nm-thick shell around the bubble. He atoms were not detected in the APT analysis, likely due to the He gas rapidly escaping the sample into the APT vacuum chamber as the bubble opened during the field evaporation process.

By comparing Fig. 4a and 4b, it is clear that Cr in NiCoCr has a larger and wider depletion around bubbles than Fe in NiCoFe. The minimum Cr concentration along the 1D profile is close to 10 at. %, and Cr does not return to the bulk concentration (33.3 at. %) until it is ~15 nm or even farther away from the bubble center. In contrast, the minimum concentration of Fe is about 15 at. % and the Fe depletion disappears at ~10 nm away from the bubble center. The larger and wider depletion of Cr compared with Fe suggests that vacancies have a larger diffusivity via Cr than via Fe, providing a fast path for vacancies to migrate to bubbles and accelerating the bubble growth in NiCoCr. Note that although the depletions of Cr and Fe are obviously different as shown by the APT analyses, it would be challenging to discover such a difference via conventional STEM-based EDS or EELS, considering that the nanosized bubbles are buried in 80 nm-thick TEM specimens.

The segregation trend observed experimentally matches well with migration energy barriers determined from *ab initio* calculations. Based on density function theory (DFT), Zhao et al. calculated the average migration barriers of point defects in NiCoCr and NiCoCrFe [34]. In both alloys, Cr and Fe consistently have a lower vacancy migration barrier than Ni and Co; thus, Cr and Fe should be depleted near bubbles. In addition, in NiCoCrFe the average migration barrier for Cr vacancies (0.580 eV) is even lower than that of Fe (0.777 eV), which suggests that vacancies diffuse even faster via Cr sites and explains the larger bubble size and swelling in NiCoCr compared to NiCoFe. When examining the electronic structure of NiCoCr, the *ab initio* calculations have revealed that the partially filled 3*d* orbitals of Cr provides larger flexibility to deform the charge distribution of Cr and hence facilitate defect migration via Cr sites [34,35].

To provide more quantitative demonstration, we calculated the chemical segregation profiles near a single bubble in both MEAs based on a classic rate theory model developed by Wiedersich et al. [36]. The governing equations for the segregation calculation include:

$$\frac{\partial c_V}{\partial t} = G + R - \nabla J_V = G + R - \nabla \left[-(\sum_{i=1}^3 d_{a_i V} C_{a_i}) \nabla C_V + \sum_{i=1}^3 (d_{a_i V} C_V \nabla C_{a_i}) \right]$$
 (1)

$$\frac{\partial C_I}{\partial t} = G + R - \nabla J_I = G + R - \nabla \left[-\left(\sum_{i=1}^3 d_{a_i I} C_{a_i}\right) \nabla C_I - \sum_{i=1}^3 (d_{a_i I} C_I \nabla C_{a_i}) \right]$$
 (2)

$$\frac{\partial c_{a_1}}{\partial t} = -\nabla J_{a_1} = \nabla \left[d_{a_1 V} \left(C_V \nabla C_{a_1} - C_{a_1} \nabla C_V \right) + d_{a_1 I} \left(C_I \nabla C_{a_1} + C_{a_1} \nabla C_I \right) \right]$$
(3)

$$\frac{\partial c_{a_2}}{\partial t} = -\nabla J_{a_2} = \nabla \left[d_{a_2 V} \left(C_V \nabla C_{a_2} - C_{a_2} \nabla C_V \right) + d_{a_2 I} \left(C_I \nabla C_{a_2} + C_{a_2} \nabla C_I \right) \right] \tag{4}$$

Here, C(x,t) is the atomic concentration of one kind of point defect or element, G is the point defect generation rate, R is the point defect recombination rate, and I is the species flux. The subscript V, I, a_i represents vacancy, interstitial, and element type, respectively. Since both MEAs are ternary, i varies from 1 to 3. The partial diffusivity of vacancy and interstitial via element a_i is represented by d_{a_iV} and d_{a_iI} , respectively. Because the sum of the three element concentrations is always

conserved, i.e., $\sum_{i=1}^{3} C_{a_i}(x,t) = 100 \ at.\%$, only four partial differential equations are needed to solve the concentrations of five species, including vacancy, interstitial, and three elements. The point defect generation rate is $G=\Gamma\eta$, where Γ is the dose rate and η is the damage efficiency. According to SRIM calculations, the average radiation dose in the analyzed region (50nm-350nm below the sample surface) is around 0.8 dpa, so the dose rate is $\Gamma=3.2\times10^{-4}$ dpa/s. The damage efficiency is estimated to be 3% based on previous studies and the fact that other defect sinks are ignored in this calculation [37]. The recombination rate is $R=\frac{4\pi r_0}{V_0}\sum_{i=1}^3(d_{a_iV}C_{a_i}+d_{a_iI}C_{a_i})C_VC_I$. Here V_0 is the atomic volume and r_0 is the point defect recombination radius, which is taken as the distance between the closest packed planes in the fcc structure. Both V_0 and r_0 can be calculated using the lattice constant, which is 3.56 Å for NiCoCr and 3.58 Å for NiCoFe [38].

The rate theory equations were solved for the time domain $0 < t < t_0$ and space domain $0 < t < t_0$. Here $t_0 = 2500$ s is the total irradiation time, $t_0 = 1$ is the location of bubble surface, and $t_0 = 2000 r_0$ indicates a boundary that is far away from the bubble where the influence of the bubble on the concentration profile is minimum and the local concentration curvature can be taken as zero, i.e., $\frac{dC_{a_1}(x_0,t)}{dx} = \frac{dC_V(x_0,t)}{dx} = \frac{dC_I(x_0,t)}{dx} = 0$. In our calculation, the bubble surface is regarded as a perfect sink; thus, defect concentrations at the bubble surface always maintain the thermal equilibrium values, i.e., $C_V(0, t) = \exp\left(-\frac{E_V^f}{k_B T}\right)$, $C_I(0, t) = \exp\left(-\frac{E_I^f}{k_B T}\right)$. The boundary conditions for element concentration at the bubble surfaces are taken as $\frac{dC_{a_1}(0,t)}{dx} = 0$. For the initial conditions, the point defect concentrations are set to the thermal equilibrium values and the element concentrations are set to 33.3 at.%. The most important parameter for the calculation is the defect partial diffusivity, $d_{a_iV/I}$, which is calculated using the equation below

$$d_{a_iV/I} = d_0 \exp(-\frac{E_{a_iV/I}^m}{k_B T}).$$
 (5)

The pre-exponential factor is $d_0 = \frac{1}{6}a^2Zv = a_0^2v$, where a is the distance between nearest neighbor sites, Z is the number of possible jump sites, and v is a constant jump attempt frequency taken as 1×10^{12} Hz here. In the fcc structure, Z=12 and $a=\frac{\sqrt{2}}{2}a_0$, where a_0 is the lattice constant. $E_{a_iv/l}^m$ is the average migration energy barrier of either vacancy or interstitial via element a_i . To the best of our knowledge, DFT-calculated $E_{a_iv/l}^m$ values are only available for NiCoCr and NiCoCrFe, but not for NiCoFe. To estimate the effective migration barriers of Fe point defects in NiCoFe, we calculated the differences in migration barriers between Cr and Fe point defects in NiCoFe, and then add the differences to $E_{a_iv/l}^m$ of Cr in NiCoCr. The effective $E_{a_iv/l}^m$ values in NiCoFe are consistent with the fact that Cr vacancies diffuse faster than Fe vacancies as demonstrated by the DFT calculations. The $E_{a_iv/l}^m$ values used in our calculations are summarized in Table 2. A sensitivity analysis of the $E_{Fe,v}^m$ value for the segregation calculation was performed and discussed in Supplementary Note 7. To directly compare with the experimental results, the calculated profiles were averaged over 1 nm distances, which was similar to how the experimental concentration profiles were obtained. Also, the concentration values at the bubble surface were taken as the concentration values inside the bubble, i.e., -4 nm to 4 nm in Fig. 4.

Fig. 4c and 4d show the calculated elemental concentration profiles near a single bubble in NiCoCr and NiCoFe, respectively. It is clear that the lower vacancy migration barrier via Cr compared to Fe leads to a larger and wider depletion of Cr near bubbles. This trend matches well with experimental measurements shown in Fig. 4a and 4b. Combining the APT experiments and the rate theory calculations, we can conclude that vacancies migrate faster via Cr in NiCoCr than via Fe in NiCoFe, and this fast vacancy migration leads to an accelerated bubble growth rate and

a larger swelling in NiCoCr. Note that the current rate theory calculations cannot fully reproduce the experimental concentration profiles. For example, the calculated magnitude of Cr or Fe depletion does not match the experimental results. Also, Co enriches more than Ni in NiCoCr according to the APT analysis (Fig. 4a), but this trend is reversed in the calculation (Fig. 4c). These discrepancies may originate from simplified assumptions in the current rate theory calculation: the bubble surfaces are regarded as perfect sinks; the point defect loss to other sinks, such as dislocations, are ignored; we consider the inverse Kirkendall effect as the governing mechanism for the element segregation near bubbles and ignore the possible defect dragging effect; the difference in migration entropies of different alloy elements is ignored. Future studies are needed for more sophisticated models to calculate segregation near bubbles. Nevertheless, the agreement in the depletion trend of Fe and Cr between our experiment and calculation provides strong evidence for the element effect on vacancy migration and bubble growth in MEAs.

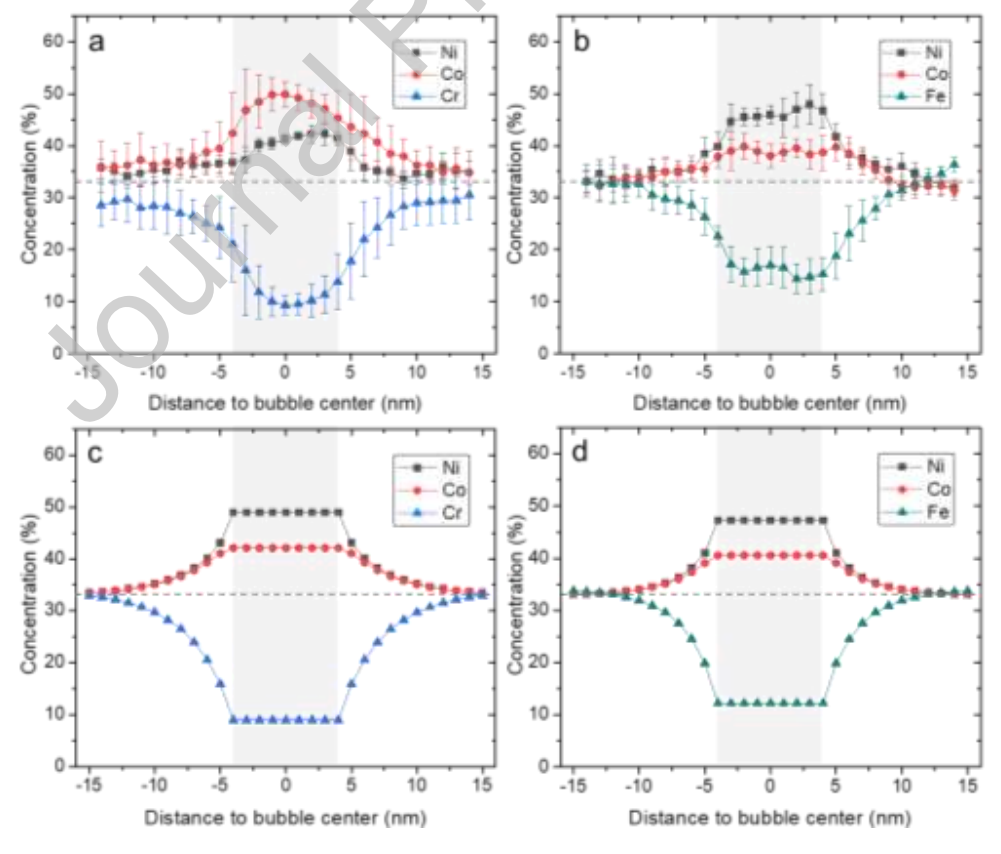


Figure 4. Elemental segregation near bubbles in two MEAs. (a) APT measured composition profiles in NiCoCr and (b) NiCoFe. Standard deviations of multiple local composition values are error bars in the profile. (c) Rate-theory calculated composition profiles in NiCoCr and (d) NiCoFe. Shaded region between -4 nm to 4 nm in each figure indicates the bubble location. The horizontal dashed line in each figure indicates the ideal bulk concentration of elements in the ternary alloy, i.e., 33.3 at. %.

Table 2. Defect migration energies of interstitials and vacancies for rate theory calculation according to DFT calculated [34].

		NiCoCr			NiCoFe	
-	Ni	Co	Cr	Ni	Со	Fe
$E_{I}^{m}\left(eV\right)$	0.200	0.221	0.127	0.200	0.221	0.193
$E_{V}^{m}\left(eV\right)$	1.042	1.041	0.685	1.042	1.041	0.882

3.3. Chemical segregation near bubbles in HEAs

Since segregation analyses revealed the different effects of Fe and Cr on vacancy mobility and explained the accelerated bubble growth in NiCoCr, we were curious whether a similar trend could be found when comparing Mn and Pd. Therefore, APT experiments were conducted in two HEAs. Five bubbles with D_{bubble} =5-9 nm were analyzed for each HEA and the average concentration profiles around bubbles in the Mn-HEA are plotted in Fig. 5a. Among all five elements, Ni and Co becomes enriched while Fe, Cr, and Mn become depleted. In particular, Mn has an obvious larger and wider depletion profile than Fe and Cr. This trend is consistent with previous segregation measurements near dislocation loops in Mn-HEAs, and can be rationalized by differences in atomic size between these elements [39]. The atomic size of an element in solid solution can be represented by the volume size-factor (VSF), which is defined as the fractional change in average atomic volume per 1 at.% concentration increase of the element in solid solution [39,40]. Using measured lattice parameters of solid solutions with varying concentrations, VSFs in many binary metal solutions have been calculated previously [40]. Table 3 summarizes the VSFs

of elements in our study calculated using Ni-based solid solutions. For elements in Mn-HEA, the VSF ranking is Mn>Fe≳Cr>Ni≳Co. Since vacancies prefer to exchange positions with oversized atoms [19], it is reasonable that vacancies migrate easier via the largest Mn, explaining the largest depletion of Mn.

Following the same logic, we would expect an even larger depletion of Pd around bubbles. Compared to other elements, Pd is in the next row of the periodic table, so its atomic volume is substantially increased, as indicated by its very large VSF (=41.33) in Table 3. However, some unexpected treads are found based on the APT segregation analysis. Fig. 5b-5d show 1D concentration profiles across three different bubbles in Pd-HEA. We can still observe the overall enrichment of Ni and Co and the depletion of Cr, Fe, and Pd, which are consistent with the fact that vacancies prefer to migrate via oversized atoms. However, the detailed distributions of Pd near bubbles appear to be quite random. For example, in Fig. 5b, the Pd concentration reaches its local minimum on both sides of the bubble; while in Fig. 5d, the Pd concentration achieves the maximum on one side of the bubble. This random nature prevented us from obtaining an average segregation profile in the Pd-HEA similar to what we did for other CSAs. In addition, unlike the behavior of Mn, the depletion of Pd is not spatially correlated with the Fe or Cr depletion. Instead, wherever Fe or Cr concentration reaches a minimum, the Pd concentration reaches a local maximum. This trend can be observed clearly at x=-1 nm in Fig. 5b, x=0 nm in Fig. 5c, and x=4nm in Fig. 5d. Correspondingly, wherever the local Pd concentration approaches its minimum, local Fe and Cr concentrations maintain relatively high levels. This indicates that Pd tends to spatially separate from Fe and Cr. This trend can be observed more obviously in the 2D element maps. Fig. 6a and 6b shows the concentration map of (Fe+Cr) and Mn in the Mn-HEA, respectively; Fig. 6c and 6d shows the concentration map of (Fe+Cr) and Pd in the Pd-HEA, respectively. A 4

nm-thick slab-shaped ROI was applied to the APT reconstruction to extract the elemental maps. The bubble location is marked by a white dashed-line circle in the maps, which was determined based on local atom density variations in the APT reconstruction. As shown in Fig. 6a and 6b, the spatial distribution of Mn, Fe, and Cr around the bubble are similar. In contrast, a comparison between Fig. 6c and 6d reveals that the distributions of Pd and (Fe+Cr) are nearly inverted. Based on the 1D and 2D segregation analyses, we can conclude that in addition to the overall depletion of oversized atoms around bubbles, the very large Pd atoms tend to further separate from other oversized atoms like Fe and Cr. To demonstrate the unique feature of element segregation was developed during the bubble formation process, 2D element maps in regions far away from bubbles in the APT reconstruction are provided in Supplementary Note 6. Note that the element distributions around bubbles in Fig. 6a and 6b are not round but dumbbell shaped. It is because the ion trajectory aberration in APT around a bubble gets to the maximum when half of the bubble is evaporated during the APT experiment, leading to the largest element intermixing in the middle of the bubble, while the aberration and element intermixing become negligible near the top and the bottom of the bubble [20]. We also noticed that in HEAs, Fe depleted more than Cr near bubbles, which was different from the trend shown in MEAs. It is possible that the oversized elements Mn and Pd modified the preferred vacancy diffusion via Cr, but future atomistic simulation is needed to understand the difference in defect mobility between MEAs and HEAs.

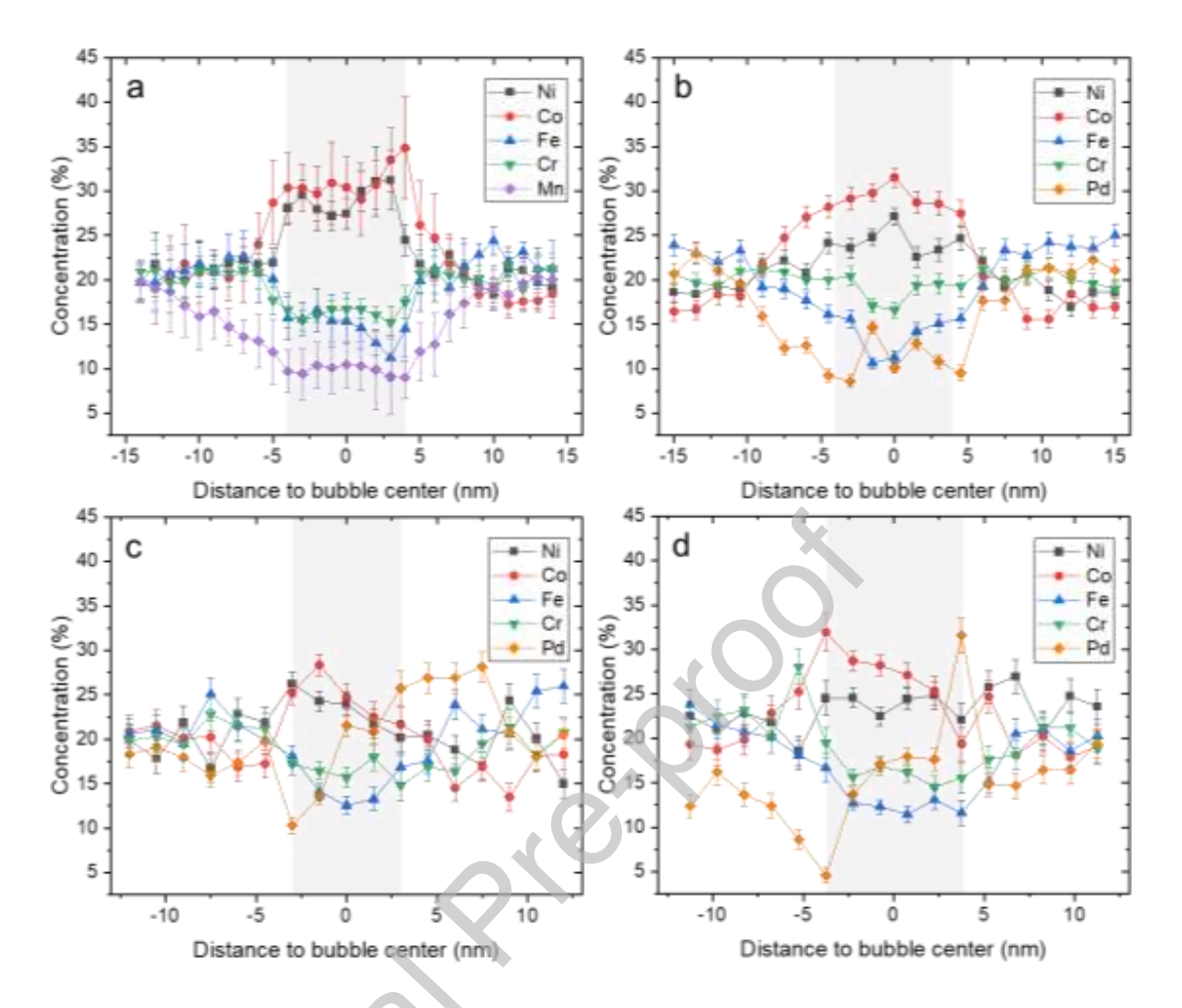


Figure 5. Elemental segregation near bubbles in two HEAs measured by APT. (a) Average composition profiles near bubbles in Mn-HEA. Standard deviations of multiple local composition values are error bars in the profiles. (b-d) Composition profiles near three different bubbles in Pd-HEA. Error bars are calculated based on local atom number counts. Shaded region in each image indicates the bubble location.

Table 3. Volume size factors of different elements in Ni-based alloys and their metal atom radii. Values are taken from reference [40].

Element	Ni	Со	Cr	Fe	Mn	Pd
VSF (%)	1	1.76	10.34	10.57	23.20	41.33
Metal atom radius (Å)	1.377	1.385	1.423	1.411	1.428	1.521

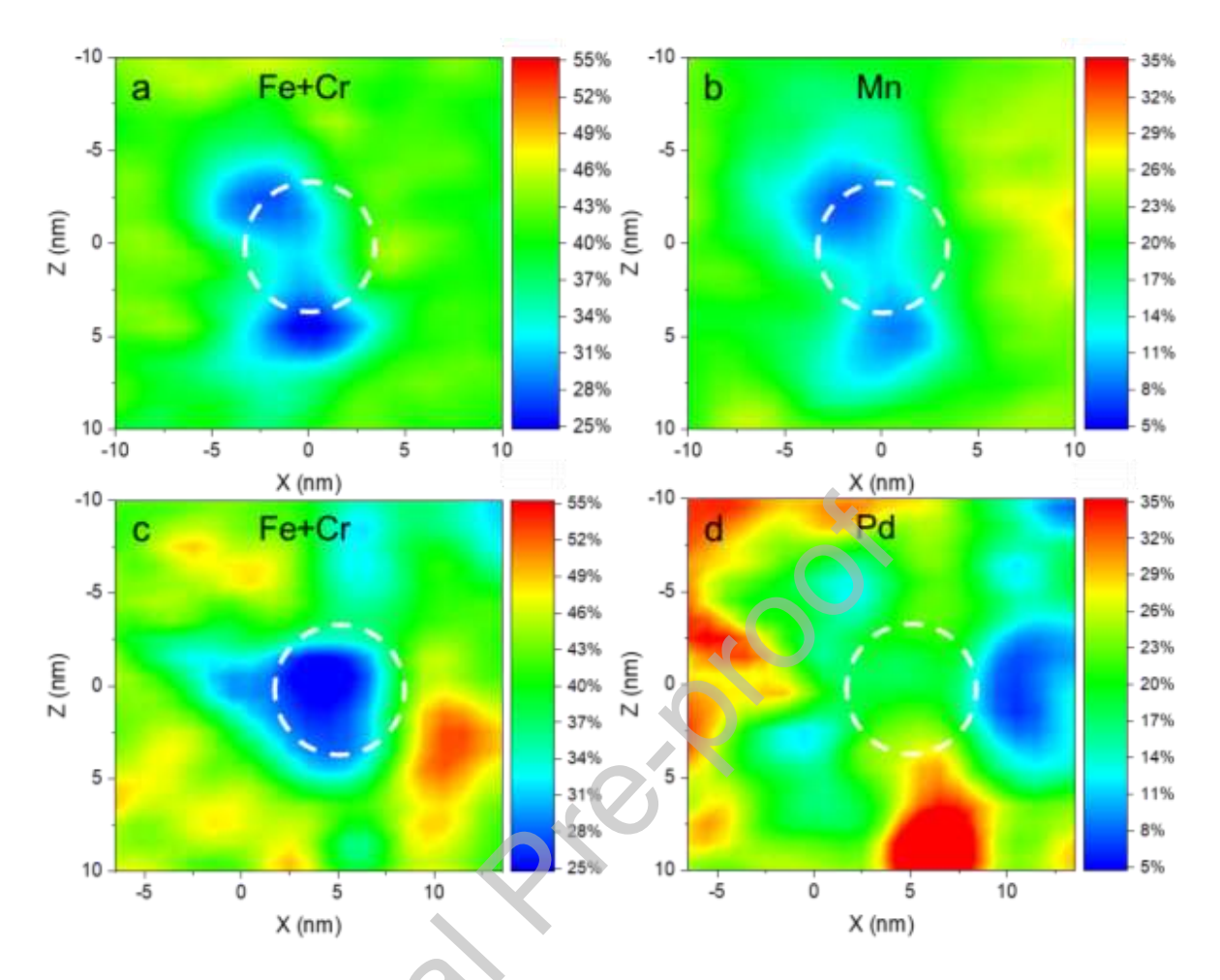


Figure 6. 2D element maps near bubbles in two HEAs. (a) Concentration of Fe+Cr and (b) Mn near a bubble in Mn-HEA. (c) Concentration of Fe+Cr and (d) Pd near a bubble in Pd-HEA. White dashed circle indicates the bubble location in each figure.

The different magnitudes of the atomic size mismatch between the two HEAs may explain the different segregation behaviors. In Mn-HEA, although Mn is the largest element in the alloy, all the elements are in the same row of the periodic table, and therefore, have relatively similar sizes. As shown in Table 3, if these elements are in pure metal status, the radius of the largest element Mn is only 3.7% larger than the smallest Ni. Therefore, oversized Mn, Cr, and Fe can deplete together near bubbles, providing an obstacle-free path for vacancies to flow towards the bubble surface and facilitating bubble growth. As a comparison, the metal atomic radius of Pd is 10.5% larger than Ni and about 7.0 % larger than Fe or Cr, thus, the atomic size mismatch in Pd-HEA is

much higher than in Mn-HEA. As vacancies flow to bubbles, oversized Pd, Fe, and Cr are transported away while undersized Ni and Co are enriched around bubbles. However, because of the high degree of atomic size mismatch, the regions enriched with undersized Ni and Co become quite attractive to the massively large Pd atoms, so it will drive Pd to migrate back, aggregate locally, and further separate Pd from Fe and Cr. Since Pd is an oversized atom, the local aggregation of Pd around bubbles is achieved by vacancy migration away from the bubble, which will deviate the vacancy flux toward the bubble surface and decelerate bubble growth. The higher tendency for chemical separation in Pd-HEA than Mn-HEA was also identified in a recent study based on STEM-EDS analysis [41]. Note that in addition to the high degree of atomic size mismatch, studies also suggested that differences in electronegativity and chemical-affinity disparity may contribute to the high tendency for local segregation in Pd-HEA [41,42], so further investigations are needed to fully understand the underlying mechanisms. Nevertheless, our study reveals that the additional chemical separation around bubbles in Pd-HEA adds obstacles for vacancy flux to bubble surfaces and acts as an effective mechanism to suppress the bubble growth.

3.4. Mechanisms for suppressing bubble growth by alloy chemical complexity

Several mechanisms have been proposed to explain the increased resistance to bubble formation introduced by alloy chemical complexity. First, the complicated defect energy landscape in CSAs modifies the defect kinetics. Specifically, interstitial mobility is substantially reduced while the vacancy mobility is enhanced, which reduce the mobility gap between Frenkel pairs and promote their recombination; hence, fewer vacancies are available for bubble growth [12,35,43]. Second, the complicated chemical environment helps slow down He diffusion and traps He atoms as small clusters [44,45]. Third, the alloy chemical complexity can restrict the evolution and emission of dislocations around bubbles, leading to higher He densities inside bubbles and smaller

bubble sizes [33]. These mechanisms may work cooperatively and contribute together to the lower bubble growth rate in more chemically complicated alloys. In this study, we also find experimental evidence supporting some of the mechanisms above. Fig. 7 compares TEM images acquired under a two-beam condition showing dislocations and dislocation loops generated by the He ion irradiation. These BF-TEM images were acquired from a region 50 nm – 350 nm below the irradiated surface, the same region where bubbles were counted and analyzed in this study. The average size of dislocation loops in each sample was measured and summarized in Table 1. To be noted, the sizes of dislocation loops were determined by measuring the longest axis. According to Fig. 7 and Table 1, as the number of alloy elements increases, the lengths of dislocations and loops shorten. Considering the high binding energy of He atoms to vacancies [46], it is reasonable to assume that the majority of vacancies cluster with He atoms, so the dislocations and loops are mostly interstitial-type in Fig. 7. Therefore, smaller loop sizes indicate that the interstitial mobility is lower and Frankel pairs recombine more efficiently in alloys with higher chemical complexity, which is consistent with previous studies and the overall trend of the suppression of bubble growth in MEAs and HEAs [8].

However, the mechanisms above cannot fully explain the trend of bubble growth and swelling observed in our study. For example, a comparison between Fig. 7b and 7e shows that the average loop size in Mn-HEA is obviously smaller than that in NiFe, suggesting a lower interstitial mobility and enhanced Frenkel pair recombination in the Mn-HEA. However, the swelling of the Mn-HEA is much higher than NiFe. Also, as shown in Fig. 7c and 7d, dislocation loops in the two MEAs exhibit similar morphologies and size distributions, but the bubbles in these alloys have quite different average sizes. Therefore, in addition to the factors identified by previous studies, our study indicates that the vacancy flux to bubbles mediated by the alloying elements also

significantly impacts bubble growth in CSAs. A reduction in the vacancy migration barrier can facilitate point defect recombination; however, if vacancies diffuse too fast via certain alloying elements, it will eventually accelerate vacancy clustering and bubble growth, as shown for NiCoCr and Mn-HEA. A deliberate tuning of vacancy flow using alloy chemical complexity is necessary to optimize the overall radiation resistance of CSAs. Two promising approaches are identified here to achieve this goal. The first is to choose alloying elements that only moderately increase the vacancy mobility, e.g., Fe to CSAs. The second approach is to utilize the local chemical separation introduced by massive atomic size mismatch, e.g., in Pd-HEA, so the vacancy flux to bubble surfaces can be deflected and bubble growth is suppressed. In addition, our study also indicates that increasing alloy chemical complexity does not simply mean mixing more alloying elements. The variations in electronic and atomic structures introduced by certain types of alloying elements, such as the partially filled 3d orbitals of Cr and the massive atomic size mismatch introduced by Pd, play a more critical role in modifying the defect energy landscape, tuning the defect mobility, and controlling the alloy resistance to radiation damage.

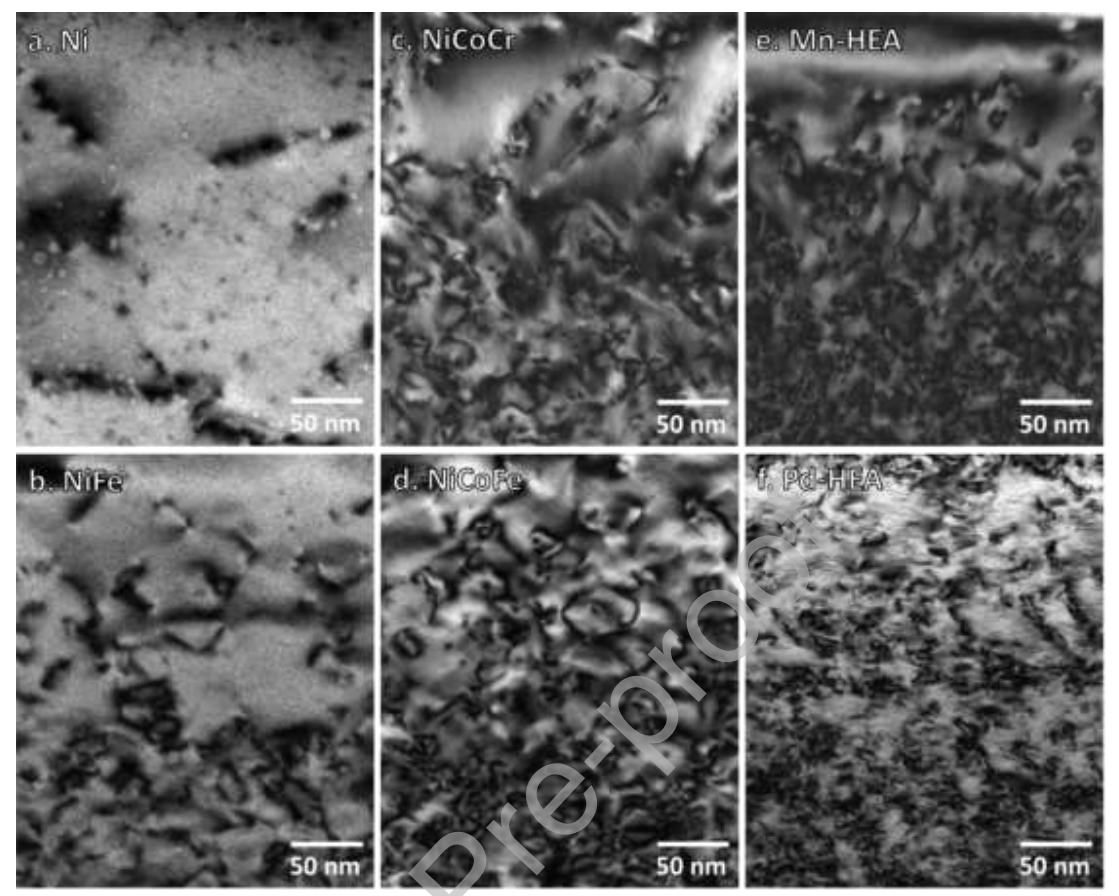


Figure 7. BF-TEM images acquired under the two-beam condition with $\mathbf{g} = (200)$ showing dislocations and loops in Ni and five CSAs. (a-d) were acquired near <100> zone axis and (e-f) were near <110> zone axis. In each image, top edge is ~50 nm below the irradiated sample surface and bottom edge is ~350 nm below the surface.

It is worth mentioning that a few key factors that may affect the bubble formation in Ni-based CSAs were not examined in this study. Frist, the diffusion of He atoms plays a critical role in the bubble nucleation and growth process [11], but so far it is not clear how chemical complexity can modify the diffusivity of He in Ni-based CSAs. Second, the diffusion of vacancy clusters was not included in our discussion. Recent research revealed that in CSAs containing Ni, Cr and Fe, the mobility of small vacancy clusters was increased while the mobility of large vacancy clusters was reduced when compared to Ni, which may contribute to the lower bubble growth rate in these CSAs than Ni [47]. Third, the configuration entropy in HEAs would help increase the concentration of stable vacancy clusters [48], facilitating the formation of small and dense bubbles

in HEAs. Future studies are necessary to systematically understand the effects of all these factors on bubble nucleation and growth in CSAs.

4. Conclusion

We investigated the effects of chemical complexity on He bubble formation and swelling by comparing Ni and Ni-based CSAs containing different numbers and types of elements. Our analyses demonstrate that an improved resistance to bubble formation cannot be achieved simply by increasing the number of alloying elements. Attention should be paid to the tunable chemical complexity at the levels of electrons and atoms, and bubble formation is more efficiently suppressed with specific CSA chemistries. Based on the elemental segregation analysis combining APT characterization and rate theory calculation, we show that the vacancy flux toward bubbles tuned by the alloying elements plays a major role in controlling the bubble growth. More specifically, the larger vacancy mobility via Cr contributes to a higher swelling in NiCoCr than NiCoFe and NiFe. In addition, the atomic size mismatch introduced by massive Pd atoms leads to the separation of Pd from other oversized elements like Fe and Cr around bubbles, which effectively deflects the vacancy flux away from bubbles and suppresses bubble growth. To design CSAs with superior radiation resistance, it is necessary to carefully choose alloy elements so the vacancy mobility is optimized.

Copyright Notice

This manuscript has been authored by UT-Battelle, LLC under Contract No. DE-AC05-00OR22725 with the U.S. Department of Energy (DOE). The US government retains and the publisher, by accepting the article for publication, acknowledges that the US government retains a nonexclusive, paid-up, irrevocable, world-wide license to publish or reproduce the published form

of this manuscript, or allow others to do so, for US government purposes. DOE will provide public access to these results of federally sponsored research in accordance with the DOE Public Access Plan (http://energy.gov/downloads/doe-public-access-plan).

Acknowledgment

This work was supported by the Energy Dissipation to Defect Evolution (EDDE) Center, an Energy Frontier Research Center funded by the U.S. Department of Energy (DOE), Office of Science, Basic Energy Sciences under contract number DE-AC05-00OR22725. Electron microscopy and APT were conducted at Oak Ridge National Laboratory's Center for Nanophase Materials Sciences (CNMS), which is a U.S. DOE Office of Science User Facility. Helium implantations were supported by the Center for Integrated Nanotechnologies (CINT), an Office of Science User Facility operated for the U.S. Department of Energy (DOE) Office of Science. Los Alamos National Laboratory, an affirmative action equal opportunity employer, is managed by Triad National Security, LLC for the U.S. Department of Energy's NNSA, under contract 89233218CNA000001. The authors would like to thank James Burns for assistance in running the APT experiments.

Author credit statement

Xing Wang: Conceptualization, methodology, microscopy analysis, rate-theory calculation, and writing. **Ke Jin**: Sample fabrication. **Chun-Yin Wong**: Developing machine learning model for automated bubble measurement. **Di Chen**: Ion irradiation. **Hongbin Bei**: Sample fabrication. **Yongqiang Wang**: Ion irradiation. **Maxim Ziatdinov**: Developing machine learning model for automated bubble measurement. **William J. Weber**: Conceptualization, methodology, and editing. **Yanwen Zhang**: Conceptualization, methodology, and editing. **Jonathan Poplawsky**: Atom probe tomography analysis and editing. **Karren**

L. More: Conceptualization, methodology, microscopy analysis, and writing. All authors contributed to manuscript review.

Declaration of interests

The authors declare that they have no known competing financial interests or personal relationships that could have appeared to influence the work reported in this paper.

Reference

- [1] I.J. Beyerlein, A. Caro, M.J. Demkowicz, N.A. Mara, A. Misra, B.P. Uberuaga, Radiation damage tolerant nanomaterials, Mater. Today. 16 (2013) 443–449. https://doi.org/10.1016/j.mattod.2013.10.019.
- [2] K. Yutani, H. Kishimoto, R. Kasada, A. Kimura, Evaluation of Helium effects on swelling behavior of oxide dispersion strengthened ferritic steels under ion irradiation, J. Nucl. Mater. 367–370 (2007) 423–427. https://doi.org/10.1016/j.jnucmat.2007.03.016.
- [3] Y. Zhang, G.M. Stocks, K. Jin, C. Lu, H. Bei, B.C. Sales, L. Wang, L.K. Béland, R.E. Stoller, G.D. Samolyuk, M. Caro, A. Caro, W.J. Weber, Influence of chemical disorder on energy dissipation and defect evolution in concentrated solid solution alloys, Nat. Commun. 6 (2015) 8736. https://doi.org/10.1038/ncomms9736.
- [4] N.A.P.K. Kumar, C. Li, K.J. Leonard, H. Bei, S.J. Zinkle, Microstructural stability and mechanical behavior of FeNiMnCr high entropy alloy under ion irradiation, Acta Mater. 113 (2016) 230–244. https://doi.org/10.1016/j.actamat.2016.05.007.
- [5] Y. Zhang, T. Egami, W.J. Weber, Dissipation of radiation energy in concentrated solid-solution alloys: Unique defect properties and microstructural evolution, MRS Bull. 44 (2019) 798–811. https://doi.org/10.1557/MRS.2019.233.
- [6] Y. Zhang, S. Zhao, W.J. Weber, K. Nordlund, F. Granberg, F. Djurabekova, Atomic-level heterogeneity and defect dynamics in concentrated solid-solution alloys, Curr. Opin. Solid State Mater. Sci. 21 (2016) 221–237. https://doi.org/10.1016/j.cossms.2017.02.002.
- [7] O. El-Atwani, N. Li, M. Li, A. Devaraj, J.K.S. Baldwin, M.M. Schneider, D. Sobieraj, J.S. Wróbel, D. Nguyen-Manh, S.A. Maloy, E. Martinez, Outstanding radiation resistance of tungsten-based high-entropy alloys, Sci. Adv. 5 (2019) 1–9. https://doi.org/10.1126/sciadv.aav2002.
- [8] T. Yang, C. Li, S.J. Zinkle, S. Zhao, H. Bei, Y. Zhang, Irradiation responses and defect behavior of single-phase concentrated solid solution alloys, J. Mater. Res. 33 (2018) 3077–3091. https://doi.org/10.1557/jmr.2018.285.
- [9] K. Jin, W. Guo, C. Lu, M.W. Ullah, Y. Zhang, W.J. Weber, L. Wang, J.D. Poplawsky, H. Bei, Effects of Fe concentration on the ion-irradiation induced defect evolution and hardening in Ni-Fe solid solution alloys, Acta Mater. 121 (2016) 365–373. https://doi.org/10.1016/j.actamat.2016.09.025.
- [10] Y. Osetsky, A. V. Barashev, L.K. Béland, Z. Yao, K. Ferasat, Y. Zhang, Tunable chemical complexity to control atomic diffusion in alloys, NPJ Comput. Mater. 2020 61. 6 (2020) 1–8. https://doi.org/10.1038/s41524-020-0306-9.

- [11] H. Trinkaus, B.N. Singh, Helium accumulation in metals during irradiation Where do we stand?, J. Nucl. Mater. 323 (2003) 229–242. https://doi.org/10.1016/j.jnucmat.2003.09.001.
- [12] D. Chen, S. Zhao, J. Sun, P. Tai, Y. Sheng, Y. Zhao, G. Yeli, W. Lin, S. Liu, W. Kai, J.J. Kai, Diffusion controlled helium bubble formation resistance of FeCoNiCr high-entropy alloy in the half-melting temperature regime, J. Nucl. Mater. 526 (2019) 151747. https://doi.org/10.1016/j.jnucmat.2019.151747.
- [13] R.W. Harrison, G. Greaves, H. Le, H. Bei, Y. Zhang, S.E. Donnelly, Chemical effects on He bubble superlattice formation in high entropy alloys, Curr. Opin. Solid State Mater. Sci. 23 (2019) 100762. https://doi.org/10.1016/j.cossms.2019.07.001.
- [14] X. Wang, K. Jin, D. Chen, H. Bei, Y. Wang, W.J. Weber, Y. Zhang, K.L. More, Effects of Fe concentration on helium bubble formation in NiFex single-phase concentrated solid solution alloys, Materialia. 5 (2019) 100183. https://doi.org/10.1016/J.MTLA.2018.100183.
- [15] K. Jin, C. Lu, L.M. Wang, J. Qu, W.J. Weber, Y. Zhang, H. Bei, Effects of compositional complexity on the ion-irradiation induced swelling and hardening in Ni-containing equiatomic alloys, Scr. Mater. 119 (2016) 65–70. https://doi.org/10.1016/j.scriptamat.2016.03.030.
- [16] Z. Fan, S. Zhao, K. Jin, D. Chen, Y.N. Osetskiy, Y. Wang, H. Bei, K.L. More, Y. Zhang, Helium irradiated cavity formation and defect energetics in Ni-based binary single-phase concentrated solid solution alloys, Acta Mater. 164 (2019) 283–292. https://doi.org/10.1016/j.actamat.2018.10.040.
- [17] A.J. Ardell, P. Bellon, Radiation-induced solute segregation in metallic alloys, Curr. Opin. Solid State Mater. Sci. 20 (2016) 115–139. https://doi.org/10.1016/j.cossms.2015.11.001.
- [18] K.G. Field, L.M. Barnard, C.M. Parish, J.T. Busby, D. Morgan, T.R. Allen, Dependence on grain boundary structure of radiation induced segregation in a 9 wt.% Cr model ferritic/martensitic steel, J. Nucl. Mater. 435 (2013) 172–180. https://doi.org/10.1016/j.jnucmat.2012.12.026.
- [19] P.R. Okamoto, L.E. Rehn, Radiation-induced segregation in binary and ternary alloys, J. Nucl. Mater. 83 (1979) 2–23. https://doi.org/10.1016/0022-3115(79)90587-7.
- [20] X. Wang, C. Hatzoglou, B. Sneed, Z. Fan, W. Guo, K. Jin, D. Chen, H. Bei, Y. Wang, W.J. Weber, Y. Zhang, B. Gault, K.L. More, F. Vurpillot, J.D. Poplawsky, Interpreting nanovoids in atom probe tomography data for accurate local compositional measurements, Nat. Commun. 11 (2020) 1022. https://doi.org/10.1038/s41467-020-14832-w.
- [21] Z. Wu, Y.F. Gao, H. Bei, Single crystal plastic behavior of a single-phase, face-center-cubic-structured, equiatomic FeNiCrCo alloy, Scr. Mater. 109 (2015) 108–112. https://doi.org/10.1016/j.scriptamat.2015.07.031.
- [22] F. Menzinger, F. Sacchetti, Dose-rate dependence of swelling and damage in ion-irradiated nickel, J. Nucl. Mater. 57 (1975) 193–197. https://doi.org/10.1016/0022-3115(75)90259-7.
- [23] B. Horváth, R. Schäublin, Y. Dai, Flash electropolishing of TEM lamellas of irradiated tungsten, Nucl. Instruments Methods Phys. Res. Sect. B Beam Interact. with Mater. Atoms. 449 (2019) 29–34. https://doi.org/10.1016/j.nimb.2019.04.047.
- [24] C. Lu, L. Niu, N. Chen, K. Jin, T. Yang, P. Xiu, Y. Zhang, F. Gao, H. Bei, S. Shi, M.-R. He, I. Robertson, W.J. Weber, L. Wang, Enhancing radiation tolerance by controlling defect mobility and migration pathways in multicomponent single phase alloys, Nat.

- Commun. 7 (2016) 1-8. https://doi.org/10.1038/ncomms13564.
- [25] O. Ronneberger, P. Fischer, T. Brox, U-Net: Convolutional Networks for Biomedical Image Segmentation, in: N. Navab, J. Hornegger, W.M. Wells, A.F. Frangi (Eds.), Med. Image Comput. Comput. Interv., Springer International Publishing, Munich, Germany, 2015: pp. 234–241.
- [26] H.R. Zhang, R.F. Egerton, M. Malac, Local thickness measurement through scattering contrast and electron energy-loss spectroscopy, Micron. 43 (2012) 8–15. https://doi.org/10.1016/j.micron.2011.07.003.
- [27] M.K. Miller, R.G. Forbes, Atom Probe Tomography and the Local Electrode Atom Probe, 1st ed., Springer, New York, 2014.
- [28] J.F. Ziegler, M.D. Ziegler, J.P. Biersack, SRIM The stopping and range of ions in matter (2010), Nucl. Instruments Methods Phys. Res. Sect. B Beam Interact. with Mater. Atoms. 268 (2010) 1818–1823. https://doi.org/10.1016/j.nimb.2010.02.091.
- [29] S.M. Hafez Haghighat, G. Lucas, R. Schäublin, State of a pressurized helium bubble in iron, EPL. 85 (2009). https://doi.org/10.1209/0295-5075/85/60008.
- [30] R.S. Nelson, D.J. Mazey, R.S. Barnes, The thermal equilibrium shape and size of holes in solids, Https://Doi.Org/10.1080/14786436508211927. 11 (2006) 91–111. https://doi.org/10.1080/14786436508211927.
- [31] F. Zhang, L. Boatner, Y. Zhang, D. Chen, Y. Wang, L. Wang, Swelling and Helium Bubble Morphology in a Cryogenically Treated FeCrNi Alloy with Martensitic Transformation and Reversion after Helium Implantation, Mater. 2019, Vol. 12, Page 2821. 12 (2019) 2821. https://doi.org/10.3390/MA12172821.
- [32] C.W. Chen, The shapes of irradiation-produced voids in nickel, Phys. Status Solidi. 16 (1973) 197–210. https://doi.org/10.1002/PSSA.2210160121.
- [33] F. Granberg, X. Wang, D. Chen, K. Jin, Y. Wang, H. Bei, W.J. Weber, Y. Zhang, K.L. More, K. Nordlund, F. Djurabekova, Origin of increased helium density inside bubbles in Ni(1-x)Fex alloys, Scr. Mater. 191 (2021) 1–6. https://doi.org/10.1016/j.scriptamat.2020.08.051.
- [34] S. Zhao, T. Egami, G.M. Stocks, Y. Zhang, Effect of d electrons on defect properties in NiCoCr and NiCoFeCr concentrated solid solution alloys, Phys. Rev. Mater. 013602 (2018) 1–18. https://doi.org/10.1103/PhysRevMaterials.2.013602.
- [35] Y. Zhang, X. Wang, Y.N. Osetsky, Y. Tong, R. Harrison, S.E. Donnelly, D. Chen, Y. Wang, H. Bei, B.C. Sales, K.L. More, P. Xiu, L. Wang, W.J. Weber, Effects of 3d electron configurations on helium bubble formation and void swelling in concentrated solid-solution alloys, Acta Mater. 181 (2019) 519–529. https://doi.org/10.1016/j.actamat.2019.10.013.
- [36] H. Wiedersich, P.R. Okamoto, N.Q. Lam, A theory of radiation-induced segregation in concentrated alloys, J. Nucl. Mater. 83 (1979) 98–108. https://doi.org/10.1016/0022-3115(79)90596-8.
- [37] G.S. Was, T. Allen, Radiation-induced segregation in multicomponent alloys: Effect of particle type, Mater. Charact. 32 (1994) 239–255. https://www-sciencedirectcom.ezaccess.libraries.psu.edu/science/article/pii/1044580394901015?via%3Dihub (accessed April 27, 2021).
- [38] Y.Y. Zhao, T.G. Nieh, Correlation between lattice distortion and friction stress in Nibased equiatomic alloys, Intermetallics. 86 (2017) 45–50. https://doi.org/10.1016/j.intermet.2017.03.011.

- [39] W.Y. Chen, J.D. Poplawsky, Y. Chen, W. Guo, J.W. Yeh, Irradiation-induced segregation at dislocation loops in CoCrFeMnNi high entropy alloy, Materialia. 14 (2020) 100951. https://doi.org/10.1016/j.mtla.2020.100951.
- [40] H.W. King, Quantitative size-factors for metallic solid solutions, J. Mater. Sci. 1 (1966) 79–90. https://doi.org/10.1007/BF00549722.
- [41] Q. Ding, Y. Zhang, X. Chen, X. Fu, D. Chen, S. Chen, L. Gu, F. Wei, H. Bei, Y. Gao, M. Wen, J. Li, Z. Zhang, T. Zhu, R.O. Ritchie, Q. Yu, Tuning element distribution, structure and properties by composition in high-entropy alloys, Nature. 574 (2019) 223–227. https://doi.org/10.1038/s41586-019-1617-1.
- [42] S. Chen, Z.H. Aitken, S. Pattamatta, Z. Wu, Z.G. Yu, R. Banerjee, D.J. Srolovitz, P.K. Liaw, Y.W. Zhang, Chemical-Affinity Disparity and Exclusivity Drive Atomic Segregation, Short-Range Ordering, and Cluster Formation in High-Entropy Alloys, Acta Mater. 206 (2021) 116638. https://doi.org/10.1016/j.actamat.2021.116638.
- [43] S. Liu, D. Chen, S. Zhao, W. Lin, F. Meng, Y. Zhao, G. Yeli, F. He, Y. Li, H. Niu, J. jung Kai, Temperature-dependent helium induced microstructural evolution in equiatomic NiCo and NiFe concentrated solid solution alloys, J. Nucl. Mater. 545 (2021) 152715. https://doi.org/10.1016/j.jnucmat.2020.152715.
- [44] O. El-Atwani, A. Alvarado, K. Unal, S. Fensin, J.A. Hinks, G. Greaves, J.K.S. Baldwin, S.A. Maloy, E. Martinez, Helium implantation damage resistance in nanocrystalline W-Ta-V-Cr high entropy alloys, Mater. Today Energy. 19 (2021). https://doi.org/10.1016/j.mtener.2020.100599.
- [45] S. Zhao, D. Chen, J.J. Kai, First-principles study of He behavior in a NiCoFeCr concentrated solid–solution alloy, Mater. Res. Lett. 7 (2019) 188–193. https://doi.org/10.1080/21663831.2019.1574926.
- [46] K. Morishita, R. Sugano, B.D. Wirth, T. Diaz de la Rubia, Thermal stability of helium-vacancy clusters in iron, Nucl. Instruments Methods Phys. Res. Sect. B Beam Interact. with Mater. Atoms. 202 (2003) 76–81. https://doi.org/10.1016/S0168-583X(02)01832-3.
- [47] S. Zhao, G. Velisa, H. Xue, H. Bei, W.J. Weber, Y. Zhang, Suppression of vacancy cluster growth in concentrated solid solution alloys, Acta Mater. 125 (2017) 231–237. https://doi.org/10.1016/j.actamat.2016.11.050.
- [48] Z. Wang, C.T. Liu, P. Dou, Thermodynamics of vacancies and clusters in high-entropy alloys, Phys. Rev. Mater. 1 (2017) 043601. https://doi.org/10.1103/PHYSREVMATERIALS.1.043601/FIGURES/4/MEDIUM.